The laminar interactions of a pair of vortex tubes with a free surface

By DOUGLAS G. DOMMERMUTH

Naval Hydrodynamics Division, Science Applications International Corporation,
10260 Campus Point Dr., MS C4, San Diego, CA 92121, USA

A fully nonlinear numerical method is developed to study the viscous interactions of a pair of vortex tubes rising toward a free surface. The numerical theory uses Helmholtz's decomposition to treat the irrotational and vortical components of the flow as separate nonlinearly coupled equations. The laminar interactions of a pair of vortex tubes with a clean free surface at intermediate Froude and Weber numbers and a low Reynolds number show two distinct phases. During the rise phase of the vortex pairs, instabilities lead to the formation of helical vorticity. The rotation of the helical vorticity around the primary vortex tubes causes an unsteady oscillation in the free-surface elevation. During the reconnection phase, the helical vortex sheets get narrower and attach themselves to the free surface. The normal connections of cross-axis vorticity with the free surface give whirls. The free-surface elevation is well correlated with the vortical pressure. The numerical results agree qualitatively with experimental measurements.

1. Introduction

The experiments of Sarpkaya & Henderson (1984) and Sarpkaya (1986) show that a pair of rising trailing-tip vortices shed by a submerged delta wing may interact with free surfaces to form striations and scars. The free-surface striations, which are normal to the wing's track, occur during the initial phases of the interaction. The scar features, which form after the striations, are two depressions that are parallel to the wing's track. At high Froude numbers Sarpkaya & Suthon (1990, 1991) observe that the free-surface displacement is large and that whirls may form in the scar region at the ends of the striations. The links among the striations, scars, and whirls are not well understood. The present numerical simulations of pairs of vortex tubes interacting with a clean free surface help to explain the flow topology. Dommermuth (1992) describes the flow topology of vortex tubes interacting with a no-slip wall which has applications to heavily contaminated free surfaces at low Froude numbers.

Figure 1 reproduces photographs from the experiments of Sarpkaya & Suthon (1990) which show the striated and scarred free-surface signature of a rising vortex pair. The axis of the vortex pair points from the bottom of the page to the top of the page. Figure 1 (*a*) shows the oval which forms above the vortex pair. This is primarily a two-dimensional feature, but there is evidence of striations forming along the axis of the vortex pair. The striations are the transverse undulations in the free-surface elevation. Figure 1 (*b*) shows the scars that form on both sides of the oval. The scars are the two longitudinal dips in the free-surface elevation. In figure 1 (*c*) the striations and scars have intensified. Figure 1 (*d*) illustrates the formation of dimples by whirls in the scar region after the oval and the striations have collapsed.
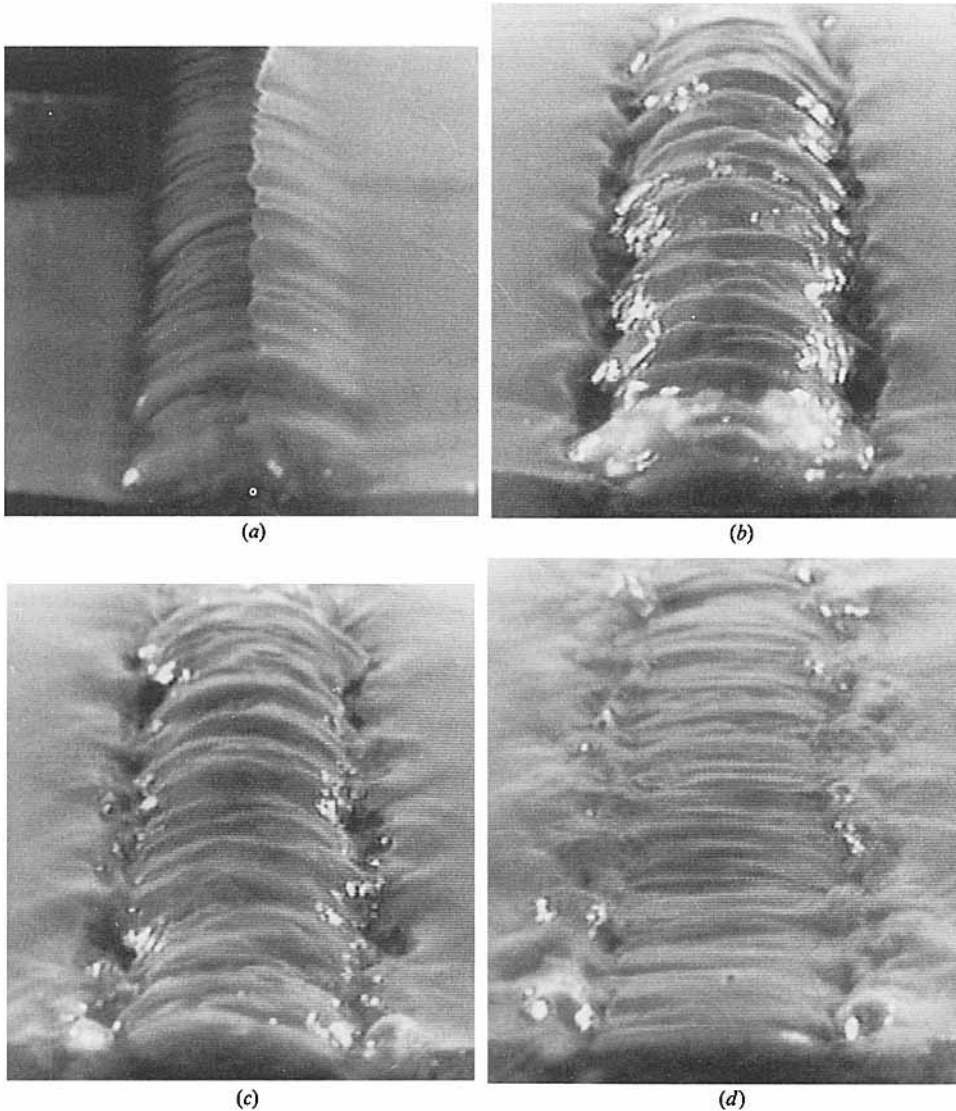
FIGURE 1. The scarred and striated signature of a vortex pair on the free surface. (a) Rise of a corrugated vortex dome; (b) formation of scars and dimples; (c) intensification of scars and striations; and (d) late stages of scar and striation formation. (These photographs are reproduced from Sarpkaya & Suthon 1990 with permission.)

Dimples on the free surface may indicate the presence of whirls. Whirls are by definition vortex tubes that are connected normal to the free surface. Sarpkaya & Suthon's observations indicate that whirls tend to form at the ends of the striations. They also observe that the striations are the manifestation of a subsurface phenomenon that occurs whether or not a free surface is present. Hirsa (1990) uses laser-induced fluorescence to show that cross-axis vortices are located below the striations that form on a dirty free surface. These cross-axis vortices are convected to the free surface by the self-induced velocity of the primary vortex pair. Hirsa's results are supported by the high-Froude-number results of Sarpkaya & Suthon (1991), who use particle traces of the free surface to show the existence of cross-axis

vorticity. Sarpkaya's (1992) studies of a turbulent vortex tube show that tentacle-like vortex sheets are thrown away from the outer edges of the vortex core. As the vortex sheets interact with the free surface, they either connect normally with the free surface or stretch out parallel to the free surface and quickly dissipate.

Ohring & Lugt (1991) and Lugt & Ohring (1992) discretize the two-dimensional Navier–Stokes equations to simulate the fully nonlinear interactions of vortex pairs with a free surface. Their numerical results illustrate the formation of ovals and scars, but not three-dimensional features such as the whirls and striations. A comprehensive review of vortices interacting with a free surface is provided by Dommermuth & Yue (1990), who have studied laminar vortex rings and tubes using linearized free-surface boundary conditions and a primitive-variable formulation of the Navier–Stokes equations. A preliminary version of the present Helmholtz formulation of the Navier–Stokes equations with linearized free-surface boundary conditions is provided in Dommermuth (1991).

2. Mathematical formulation

2.1. *Field equations*

Consider the unsteady incompressible flow of a Newtonian fluid under a free surface, and let $\boldsymbol{u} = \boldsymbol{u}(x, y, z, t) = (u, v, w)$ represent the three-dimensional velocity field as a function of time. Applying Helmholtz's theorem gives

$$\boldsymbol{u} = \boldsymbol{\nabla}\phi + \mathcal{U}, \tag{1}$$

where $\phi(x, y, z, t)$ is a velocity potential which describes the irrotational flow and $\mathcal{U}(x, y, z, t) = (U, V, W)$ is a solenoidal field which describes the vortical flow such that

$$\nabla^2 \phi = 0, \tag{2}$$

$$\boldsymbol{\nabla} \cdot \mathcal{U} = 0. \tag{3}$$

Since ϕ satisfies Laplace's equation and the divergence of the rotational field $\mathcal{U}$ is chosen to be zero, the total velocity field $\boldsymbol{u}$ conserves mass. Note that $\mathcal{U}$ may contain a portion of the irrotational field depending on how the boundary conditions are defined.

Based on this Helmholtz decomposition of the velocity field, define the total pressure Π in terms of a rotational pressure P and an irrotational pressure as follows:

$$\Pi = P - \frac{\partial \phi}{\partial t} - \tfrac{1}{2}\boldsymbol{\nabla}\phi \cdot \boldsymbol{\nabla}\phi - \frac{1}{Fr^2}z. \tag{4}$$

Here, the pressure terms are normalized by ρU_c^2 where U_c is characteristic velocity and ρ is the density. $Fr^2 = U_c^2/gL_c$ is the Froude number and L_c is the characteristic length. The vertical coordinate z is positive upward, and the origin is located at the mean free surface. Substituting these decompositions (1) and (4) into the Navier–Stokes equations gives

$$\frac{\partial \mathcal{U}}{\partial t} + ((\mathcal{U} + \boldsymbol{\nabla}\phi) \cdot \boldsymbol{\nabla}) \, \mathcal{U} + (\mathcal{U} \cdot \boldsymbol{\nabla}) \, \boldsymbol{\nabla}\phi = -\boldsymbol{\nabla}P + \frac{1}{Re} \nabla^2 \mathcal{U}. \tag{5}$$

where $Re = U_c L_c/\nu$ is the Reynolds number and ν is the kinematic viscosity.

The field equations and the boundary conditions for the velocity field can be used to deduce the rotational pressure in the fluid and the behaviour of the rotational pressure near the boundaries. For example, the divergence of the momentum

equations (5) used in combination with the mass-conservation equations (2) and (3) can be used to derive a Poisson equation for the rotational pressure. This equation expressed in indicial notation ($U_i = (U, V, W)$) is

$$\nabla^2 P = -\frac{\partial U_j}{\partial x_i}\frac{\partial U_i}{\partial x_j} - 2\frac{\partial U_j}{\partial x_i}\frac{\partial^2 \phi}{\partial x_j \partial x_i}. \tag{6}$$

Similarly, the momentum equations may also be used to prescribe the normal derivative of the rotational pressure on the boundaries of the fluid. Thus, according to the divergence theorem the rotational pressure is subject to the following solvability condition:

$$\int_S \frac{\partial P}{\partial n} = -\int_V \left(\frac{\partial U_j}{\partial x_i}\frac{\partial U_i}{\partial x_j} + 2\frac{\partial U_j}{\partial x_i}\frac{\partial^2 \phi}{\partial x_j \partial x_i}\right), \tag{7}$$

where V is a volume of fluid, S is the surface bounding the volume, and n is the unit outward-pointing normal on that surface.

2.2. Exact free-surface boundary conditions

Let the free-surface elevation be given by $z = \eta(x, y, t)$. Then define three vectors which will be used to derive an exact set of free-surface boundary conditions:

$$n = \frac{(-\eta_x, -\eta_y, 1)}{(\eta_x^2 + \eta_y^2 + 1)^{\frac{1}{2}}}, \quad t_x = \frac{(1, 0, \eta_x)}{(\eta_x^2 + 1)^{\frac{1}{2}}}, \quad t_y = \frac{(0, 1, \eta_y)}{(\eta_y^2 + 1)^{\frac{1}{2}}}, \tag{8}$$

where n is the unit normal on the free surface, and t_x and t_y are two unit tangent vectors in the (y, z)- and (x, z)-planes respectively.

The Helmholtz decomposition of the velocity field requires one additional boundary condition to be prescribed on the free surface. As will be shown, the most expedient boundary condition that can be specified is that the normal component of the rotational velocity is zero on the free surface:

$$\mathcal{U} \cdot n = \frac{-U\eta_x - V\eta_y + W}{(\eta_x^2 + \eta_y^2 + 1)^{\frac{1}{2}}} = 0. \tag{9}$$

This constraint imposed on the rotational velocity field means that the evolution of the free-surface elevation is entirely prescribed in terms of the free-surface elevation itself and the velocity potential as follows:

$$\partial \eta / \partial t + \eta_x \phi_x + \eta_y \phi_y - \phi_z = 0, \tag{10}$$

where everything is evaluated on the exact position of the free surface, $z = \eta$. If the normal derivative of the potential is chosen to be zero ($\phi_n = 0$) on all boundaries besides the free surface, then the mean free-surface elevation is conserved according to the above kinematic condition (10) and an application of Green's theorem.

In addition to the two kinematic conditions (9) and (10), there are also three stress conditions which must be satisfied on the exact position of the free surface. For later reference the total stress tensor in matrix form is:

$$\sigma = \begin{vmatrix} -\Pi + \dfrac{2}{Re}(U_x + \phi_{xx}) & \dfrac{1}{Re}(U_y + V_x + 2\phi_{xy}) & \dfrac{1}{Re}(U_z + W_x + 2\phi_{xz}) \\[2mm] \dfrac{1}{Re}(U_y + V_x + 2\phi_{xy}) & -\Pi + \dfrac{2}{Re}(V_y + \phi_{yy}) & \dfrac{1}{Re}(V_z + W_y + 2\phi_{yz}) \\[2mm] \dfrac{1}{Re}(U_z + W_x + 2\phi_{xz}) & \dfrac{1}{Re}(V_z + W_y + 2\phi_{yz}) & -\Pi + \dfrac{2}{Re}(W_z + \phi_{zz}) \end{vmatrix}, \tag{11}$$

where it should be recalled that Π is the total pressure, (U, V, W) is the rotational velocity field, and ϕ is the potential field. The normal stress on the free surface must balance with the atmospheric pressure and the surface tension:

$$\boldsymbol{n} \cdot \boldsymbol{\sigma} \cdot \boldsymbol{n}^{\mathrm{T}} = -P_{\mathrm{a}} - \frac{1}{We} \boldsymbol{\nabla} \cdot \boldsymbol{n}, \tag{12}$$

where P_{a} is the atmospheric pressure, $We = \rho U_c^2 L_c / T$ is the Weber number, T is the surface tension, and the symbol $\{\}^{T}$ denotes the transpose of a vector. The fully expanded form of the normal stress condition (12) is as follows:

$$
\begin{aligned}
&\frac{\partial \phi}{\partial t} + \tfrac{1}{2} \boldsymbol{\nabla} \phi \cdot \boldsymbol{\nabla} \phi + \frac{1}{Fr^2} \eta - P \\[4pt]
&\quad + \frac{2}{Re(\eta_x^2 + \eta_y^2 + 1)} (W_z + \phi_{zz} - (W_y + V_z + 2\phi_{yz}) \eta_y - (W_x + U_z + 2\phi_{xz}) \eta_x \\[4pt]
&\quad + (V_y + \phi_{yy}) \eta_y^2 + (U_x + \phi_{xx}) \eta_x^2 + (V_x + U_y + 2\phi_{xy}) \eta_x \eta_y) \\[4pt]
&= -P_{\mathrm{a}} + \frac{1}{We} \frac{\eta_{xx}(1 + \eta_y^2) + \eta_{yy}(1 + \eta_x^2) - 2\eta_{xy}\eta_x\eta_y}{(1 + \eta_x^2 + \eta_y^2)^{\frac{3}{2}}}
\end{aligned}
\tag{13}
$$

Now it is clear that this boundary condition is an evolution equation for the potential evaluated on the exact position of the free surface. An interesting feature of this equation is the balancing of terms which occurs between the free-surface elevation and the rotational pressure in the steady-state limit as $Re \to \infty$ and $We \to \infty$. In this limit the free-surface elevation is given in terms of the rotational pressure, the atmospheric pressure, and the quadratic potential-flow terms:

$$\eta = F_r^2 (P - P_{\mathrm{a}} - \tfrac{1}{2} \boldsymbol{\nabla} \phi \cdot \boldsymbol{\nabla} \phi).$$

Here, the rotational pressure term corresponds to the scars and dimples that form above vortex tubes that are near the free surface.

Note that for fully nonlinear numerical simulations, wherein points are followed on the free surface as a function of time, the partial derivative with respect to time in (13) should be evaluated as a total derivative such that

$$
\begin{aligned}
&\frac{\mathrm{d} \phi}{\mathrm{d} t} + \tfrac{1}{2}(\phi_x^2 + \phi_y^2 - \phi_z^2) + (\eta_x \phi_x + \eta_y \phi_y) \phi_z + \frac{1}{Fr^2} \eta - P \\[4pt]
&\quad + \frac{2}{Re(\eta_x^2 + \eta_y^2 + 1)} (W_z + \phi_{zz} - (W_y + V_z + 2\phi_{yz}) \eta_y - (W_x + U_z + 2\phi_{xz}) \eta_x \\[4pt]
&\quad + (V_y + \phi_{yy}) \eta_y^2 + (U_x + \phi_{xx}) \eta_x^2 + (V_x + U_y + 2\phi_{xy}) \eta_x \eta_y) \\[4pt]
&= -P_{\mathrm{a}} + \frac{1}{We} \frac{\eta_{xx}(1 + \eta_y^2) + \eta_{yy}(1 + \eta_x^2) - 2\eta_{xy}\eta_x\eta_y}{(1 + \eta_x^2 + \eta_y^2)^{\frac{3}{2}}}.
\end{aligned}
\tag{14}
$$

This equation is the viscous and rotational counterpart of the inviscid equation first derived by Zakaharov (1968) for irrotational flow.

Let $\boldsymbol{\tau} = (\tau_1, \tau_2, \tau_c)$ model any applied shear stresses on the free surface such as the effects of surfactants or wind, then the balance of tangential stresses on the free surface may be expressed as:

$$\boldsymbol{t}_x \cdot \boldsymbol{\sigma} \cdot \boldsymbol{n}^{\mathrm{T}} = \boldsymbol{t}_x \cdot \boldsymbol{\tau}^{\mathrm{T}}, \qquad \boldsymbol{t}_y \cdot \boldsymbol{\sigma} \cdot \boldsymbol{n}^{\mathrm{T}} = \boldsymbol{t}_y \cdot \boldsymbol{\tau}^{\mathrm{T}}, \tag{15}$$

where the first equation is the balance of tangential stresses in the (y, z)-plane and the second corresponds to the (x, z)-plane. The fully expanded form of the tangential stress condition is:

$$\frac{1}{Re\,[(\eta_x^2 + 1)(\eta_x^2 + \eta_y^2 + 1)]^{\frac{1}{2}}}((U_z + W_x + 2\phi_{xz})(1 - \eta_x^2) - 2(U_x - W_z + \phi_{xx} - \phi_{zz})\,\eta_x$$

$$- (U_y + V_x + 2\phi_{xy})\,\eta_y - (V_z + W_y + 2\phi_{yz})\,\eta_x\,\eta_y) = \tau_x, \quad (16a)$$

$$\frac{1}{Re\,[(\eta_y^2 + 1)(\eta_x^2 + \eta_y^2 + 1)]^{\frac{1}{2}}}((V_z + W_y + 2\phi_{yz})(1 - \eta_y^2) - 2(V_y - W_z + \phi_{yy} - \phi_{zz})\,\eta_y$$

$$- (U_y + V_x + 2\phi_{xy})\,\eta_x - (U_z + W_x + 2\phi_{xz})\,\eta_x\,\eta_y) = \tau_y. \quad (16b)$$

Here, τ_x and τ_y represent the components of the applied shear stresses that are respectively in the (y, z)- and (x, z)-planes. Unlike the normal stress condition, the tangential stress conditions do not provide evolution equations; rather they describe how the diffusion terms in the momentum equations (5) behave near the free surface. As $Re \to \infty$, the free surface cannot support shear stresses and the tangential stress condition (16) no longer apply. Under these conditions the two kinematic conditions (9) and (10) and the normal stress condition (14) are sufficient to describe inviscid rotational flow with a free surface.

The rotational pressure field itself does not require the *a priori* specification of a boundary condition. Recall that the role of the rotational pressure is merely to project the rotational flow field onto a solenoidal field, and in order to be consistent with that role, the behaviour of the rotational pressure is specified using the momentum equations. Similarly, the rotational pressure is also used to enforce the kinematic condition for the rotational velocity (see (9)). Taking the dot product of the momentum equations with the unit normal on the free surface provides a Neumann boundary condition for the rotational pressure:

$$\frac{\partial P}{\partial n} = -\boldsymbol{n}\cdot\frac{\partial \mathscr{U}}{\partial t} - \boldsymbol{n}\cdot((\mathscr{U} + \nabla\phi)\cdot\nabla)\,\mathscr{U} - \boldsymbol{n}\cdot(\mathscr{U}\cdot\nabla)\,\nabla\phi + \frac{1}{Re}\boldsymbol{n}\cdot\nabla^2\mathscr{U}. \quad (17)$$

For the numerical computations, the partial derivative with respect to time is evaluated as a total derivative:

$$\frac{\partial P}{\partial n} = -\boldsymbol{n}\cdot\frac{\mathrm{d}\mathscr{U}}{\mathrm{d}t} - (\eta_x\,\phi_x + \eta_y\,\phi_y - \phi_z)\,\boldsymbol{n}\cdot\frac{\partial \mathscr{U}}{\partial z}$$

$$- \boldsymbol{n}\cdot((\mathscr{U} + \nabla\phi)\cdot\nabla)\,\mathscr{U} - \boldsymbol{n}\cdot(\mathscr{U}\cdot\nabla)\,\nabla\phi + \frac{1}{Re}\boldsymbol{n}\cdot\nabla^2\mathscr{U}. \quad (18)$$

The specification of the free-surface boundary conditions using a Helmholtz decomposition is now complete. One advantage of the Helmholtz formulation relative to a primitive-variable formulation is the natural and exact transition from (i) viscous vortical flow with one normal stress condition, two tangential stress conditions, and two kinematic conditions to (ii) inviscid vortical flow with one normal stress condition and two kinematic conditions to (iii) potential flow with one normal stress condition and one kinematic condition. As a result, depending on the type of flow, the most appropriate decomposition and boundary conditions will dominate.

2.3. *Initial conditions*

In addition to the boundary conditions, the initial free-surface elevation and the initial total-velocity field also require specification:

$$\eta(x, y, t = 0) = \eta_0(x, y), \tag{19}$$

$$\boldsymbol{u}(x, y, z, t = 0) = \boldsymbol{u}_0(x, y, z). \tag{20}$$

Once again, according to Helmholtz's theorem, the initial total-velocity field $\boldsymbol{u}_0$ can be expressed in terms of scalar ϕ_0 and vector $\boldsymbol{\psi}_0 = (\psi_x, \psi_y, \psi_z)_0$ velocity potentials:

$$\boldsymbol{u}_0 = \boldsymbol{\nabla}\phi_0 + \boldsymbol{\nabla} \times \boldsymbol{\psi}_0 \quad \text{where} \quad \boldsymbol{\nabla} \cdot \boldsymbol{\psi}_0 = 0. \tag{21}$$

The initial velocity field, like the time-dependent velocity field, is required to be solenoidal. Therefore, it can be shown by taking the divergence of (21) that ϕ_0 satisfies Laplace's equation:

$$\nabla^2 \phi_0 = 0. \tag{22}$$

Here, ϕ_0 may represent the effects of currents, the disturbances due to surface-piercing and submerged bodies, etc. A similar Poisson equation is satisfied by the vector potential $\boldsymbol{\psi}_0$ in terms of the initial vorticity field $\boldsymbol{\omega}_0$:

$$\nabla^2 \boldsymbol{\psi}_0 = -\boldsymbol{\omega}_0, \tag{23}$$

where $\boldsymbol{\omega} = (\omega_x, \omega_y, \omega_z)$ may be expressed in terms of the curl of the rotational velocity at any instant of time:

$$\boldsymbol{\omega} = \boldsymbol{\nabla} \times \mathcal{U}. \tag{24}$$

Based on this definition, the vorticity field is itself a solenoidal quantity.

If the free-surface elevation, potential field, and shear stresses are initially zero ($\eta_0 = 0$, $\phi_0 = 0$, and τ_x and $\tau_y = 0$ at $t = 0$), then the tangential components of vorticity (ω_x and ω_y) on the free surface are also zero, and according to the tangential stress condition (16) the free surface initially behaves like a free-slip wall. Suppose a free-slip wall exists on the plane $z = 0$, then by definition

$$U_z = 0, \quad V_z = 0, \quad W = 0, \quad \phi_z = 0, \tag{25}$$

where the first two equations give zero tangential stresses and the last two equations state that there is no flux across the plane $z = 0$. These boundary conditions for the velocities enable us to deduce the behaviour on the free-slip wall of the rotational pressure and vorticity, and also the initial conditions for the scalar and vector velocity potentials. For example, upon substitution of the boundary conditions (25) into the z-component of the momentum equations (5), it can be shown that $P_z = 0$, where the z-derivative of (3) has been used to eliminate the $W_{zz} = 0$ term. Similar arguments may be used to show that the vorticity vector is always normal to a free-slip wall, $\boldsymbol{\omega} = (0, 0, \omega_z)$ on $z = 0$. Finally, in regard to the initial conditions, the following relations for the vector velocity potential on the free-slip plane $z = 0$ can be derived:

$$(\psi_x)_0 = 0, \quad (\psi_y)_0 = 0, \quad \partial(\psi_z)_0/\partial z = 0, \quad \nabla^2 \boldsymbol{\psi}_0 = -(0, 0, (\omega_z)_0). \tag{26}$$

2.4. *Conservation of energy*

The vector product of the total velocity with the momentum equations (5) integrated over the fluid volume gives a formula for the conservation of energy, and the transport theorem in conjunction with divergence theorem may be used to simplify

the resulting equations. Upon substitution of the exact free-surface boundary conditions into this energy equation, the following formula may be derived:

$$\frac{\mathrm{d}}{\mathrm{d}t}\left(\int_V \tfrac{1}{2}u_i u_i + \frac{1}{2Fr^2}\int_{S_0}\eta^2\right) =$$

$$-\int_{S_0}\eta_t P_\mathrm{a} - \frac{1}{\mathrm{We}}\int_{S_0}\eta_t\,\boldsymbol{\nabla}\cdot\boldsymbol{n} - \frac{1}{Re}\int_V\left(\frac{\partial u_i}{\partial x_i}+\frac{\partial u_j}{\partial x_i}\right)\frac{\partial u_i}{\partial x_j} + \int_{S_f}\boldsymbol{u}_t\cdot\boldsymbol{\tau}, \quad (27)$$

where $u_i = (U+\phi_x, V+\phi_y, W+\phi_z)$ is the total velocity, S_f is the free surface, S_0 is the projection of the free surface onto the (x, y)-plane, and $\boldsymbol{u}_t$ is the component of total velocity that is tangent to the free surface. The first term $(\mathrm{d}E_{uu}/\mathrm{d}t)$ represents the change in kinetic energy integrated over the material volume of the fluid (V), the second term $(\mathrm{d}E_{\eta\eta}/\mathrm{d}t)$ represents the change in potential energy, the third term $(\mathrm{d}W_{P_\mathrm{a}}/\mathrm{d}t)$ represents the power input by atmospheric forcing, the fourth term $(\mathrm{d}W_\mathrm{T}/\mathrm{d}t)$ represents the power in capillary waves, the fifth term $(\mathrm{d}W_\nu/\mathrm{d}t)$ represents the power expended by viscous stresses, and the last term $(\mathrm{d}W_\tau/\mathrm{d}t)$ represents the power input by applied shear stresses. Note that the work due to stresses on all other boundaries besides the free surface is assumed to be zero.

3. Numerical formulation

The Navier–Stokes equations, and the boundary and initial conditions are discretized using fourth- and sixth-order finite differences. The two different orders of approximation are used to establish the convergence of the numerical scheme. The momentum equations (5), kinematic condition (10), and the normal stress condition (14) are integrated with respect to time using a third-order Runge–Kutta scheme. Each stage of the Runge–Kutta scheme is formulated to inhibit the accumulation of errors in the divergence of the rotational flow field (see Hirt, Nichols & Romera, 1975). The rotational pressure is used to project the rotational velocity onto a solenoidal field (3) and (6) with zero normal velocity on the free surface (9) and (18). Aliasing errors are controlled using fifth- and seventh-order upwind biasing of the convective terms for respectively the fourth- and sixth-order numerical algorithms (see Rai & Moin 1991). Similarly, fourth- and sixth-order smoothing schemes are used for the free-surface elevation and the potential evaluated on the free surface. Laplace's equation for the potential (2) and Poisson's equation for the rotational pressure (6) are solved at each stage of the Runge–Kutta scheme, and a solvability condition (7) is enforced for the rotational pressure. An iterative scheme in combination with Fourier techniques and LU decomposition is used to solve the nonlinear three-dimensional elliptic equations (see Appendix B). As shown in Appendix A, the z-coordinate is mapped onto a flat plane, and the grid is stretched to resolve the free-surface boundary layer. This mapping is applied to Laplace's equation (2), the Poisson equation for the pressure (6), the momentum equations (5), and all the boundary conditions. Free-slip boundary conditions are imposed on the plane $z = 0$ as initial conditions. If the applied shear stresses are also initially zero, this choice of initial conditions will satisfy the tangential-stress boundary conditions (16) and, as a result, the free-surface elevation will smoothly evolve from rest. Free-slip wall conditions are also used as boundary conditions on the sides and bottom of the computational domain so that only one vortex tube has to be modelled in the present simulations of a pair of vortex tubes rising toward a free surface.

4. Numerical studies

A schematic picture which illustrates the numerical simulations of a three-dimensional vortex pair rising up to a free surface is provided in figure 2. Table 1 provides the numerical parameters of six computer simulations. These computer simulations are used to establish the validity of the numerical scheme for one set of physical parameters. Owing to symmetry only one of the vortex tubes of the vortex pair is modelled. Initially this vortex tube is deeply submerged, and then the self-induced velocities of the vortex pair cause the vortex tube to rise up to the free surface. The primary objective of the present numerical simulations is to help explain the formation of striations, scars, and whirls observed in Sarpkaya & Suthon's (1990, 1991) experiments.

A Gaussian core distribution is used to specify the initial vorticity field:

$$
\left.
\begin{aligned}
(\omega_y)_0 &= \omega_c \exp\left(-[(x-x_{cen})^2+(z-z_{cen})^2]/r_c^2\right) \\
x_{cen} &= x_0 + x_{amp}\cos(y\pi/W), \quad z_{cen} = z_0 + z_{amp}\cos(y\pi/W),
\end{aligned}
\right\}
\tag{28}
$$

where ω_c is the peak vorticity, r_c is the core radius, (x_0, z_0) is the mean position of the core centre in the (x, z)-plane, and x_{amp} and z_{amp} are sinusoidal perturbations that are applied to the core position. The lengths of the computational domains along the x-, y-, and z-axes are respectively denoted L, W, and D. In terms of the initial peak vorticity and core radius the circulation is $\Gamma = \pi r_c^2 \omega_c$. This initial vorticity field is not solenoidal, but the velocity field is solenoidal, and the vorticity field that is recalculated from the initial velocity field is also solenoidal (see (21)).

As is indicated in figure 2 and table 1, the initial conditions for the vortex tube studies simulate the rise of a pair of trailing-tip vortices up to a free surface, and the sinusoidal perturbations that are applied along the axis of the vortex tube (28) simulate one half of the wavelength ($\lambda = 2W$) of the striations that are observed in Sarpkaya & Suthon's (1990, 1991) experiments (see figure 1).

The lengths of the vortex tubes ($W = 1$) relative to their spans ($s = 2x_0 = 2$) are too short to permit a long-wavelength Crow instability to occur (Crow 1970). However, the experiments of Sarpkaya & Suthon show that a short-wavelength instability dominates when the symmetric long-wavelength instability is suppressed by generating short vortex pairs ($\lambda/s < 8.6$) or by generating the vortex pairs in shallow depth ($|z_0|/s < 6$). In addition, shallow depths do not allow enough time for vortex reconnection to occur across the centre-plane. The numerical simulations presented in this paper use $|z_0|/s = 1$.

The results of Sarpkaya & Suthon's and Hirsa's experiments suggest that the striations (nearly uniform corrugations when the free-surface displacements are high) are manifestations of a short-wavelength instability. Sarpkaya & Suthon's measured histograms of the wavelengths of the striations relative to the span of the vortex pair show that $0.75 \leqslant \lambda/s \leqslant 1.25$. However, the dye experiments of Sarpkaya (1985) also suggest that the instability can occur at much longer wavelengths. The present numerical simulations of vortex tubes impinging on a free surface concentrate on $\lambda/s = 1$ because Dommermuth's (1992) numerical investigations of vortex tubes impinging on a wall show that the basic flow topology does not change for $1 \leqslant \lambda/s \leqslant 8$.

The Reynolds and Froude numbers are based on the mean half-span $\frac{1}{2}s = 1$ and the centreline velocity $U_c \equiv 2\Gamma/(\pi s) = 1$. Based on these scales, the Reynolds number is $Re = \Gamma/(\pi\nu)$, where ν is the kinematic viscosity; the Froude number is
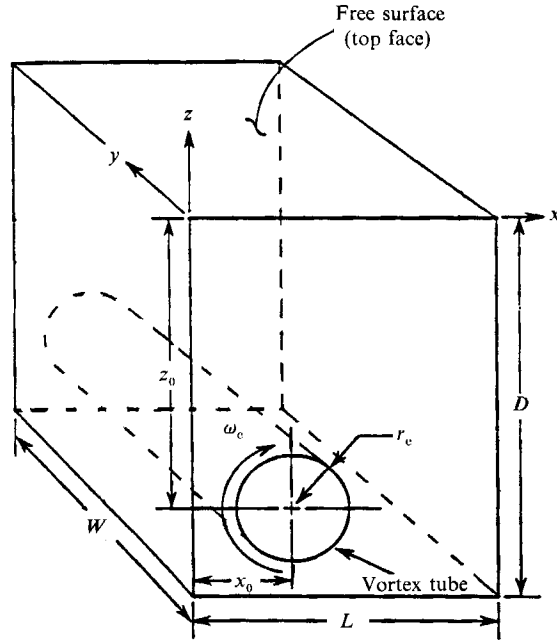
FIGURE 2. The numerical simulation of a vortex tube impinging a free surface. Symmetry boundary conditions are used on the sides and the bottom of the computational domain.

$Fr = \Gamma/(\pi g^{\frac{1}{2}} (\frac{1}{2}s)^{\frac{3}{2}})$, where g is gravity; and the Weber number is $We = 2\rho\Gamma^2/(\pi^2 sT)$, where ρ is the fluid density and T is the surface tension. The effects of surface contamination are not considered.

As noted by Sarpkaya & Suthon, the free-surface deformation is significant for $Fr^2 \geqslant 0.72$. For a flapper–plate separation of 3 cm, these Froude numbers correspond to $We \geqslant 21$ and $Re \geqslant 4900$. The Reynolds number of 200 used in the present numerical simulations is lower than Sarpkaya & Suthon's experiments, but the core radius ($r_c = 0.25$) is reasonable based on Spreiter & Sacks's (1951) analysis of trailing-tip vortices. As a result, the inviscid portion of the instability mechanism is preserved. The Froude ($Fr^2 = 0.5$) and Weber numbers ($We = 12.5$) are different from the experiments, but the ratio $Fr^2/We = 4T/(\rho g s^2) = 0.04$ is very close to the experimental values. This ratio, which corresponds to a 2.7 cm span, does not vary much in the laboratory because the experiments are performed in water using a limited range of spans. Note that higher Froude numbers lead to extreme wave slopes $O(1)$ and curvature $O(100)$ that cannot be simulated with high accuracy by the present numerical algorithm.

The perseverance of the vortex tube is investigated by adding a fluctuating velocity field to the velocity field of the vortex pair (see (28)). The generation of the fluctuating velocity field is discussed in Appendix C. The vortical pressure that is induced by the fluctuating velocity field will generate spurious high-frequency waves on the free surface unless the flow field is given sufficient time to adjust. A method for reducing these high-frequency waves is provided in Appendix D.

4.1. *Numerical results*

The spatial accuracy of the numerical simulations of vortex tubes impinging on a free surface is determined by the grid resolutions in the fluid volume and the free-surface boundary layer, and the order of the approximation. Two one-dimensional energy

Item	Run 1	Run 2	Run 3	Run 4	Run 5	Run 6
Order	sixth	fourth	fourth	fourth	fourth	fourth
Re	200	200	200	200	200	200
Fr^2	0.5	0.5	0.5	0.5	0.5	0.5
We	12.5	12.5	12.5	12.5	12.5	12.5
r_c	0.25	0.25	0.25	0.25	0.25	0.25
ω_c	16	16	16	16	16	16
x_0	1	1	1	1	1	1
z_0	-2	-2	-2	-2	-2	-2
x_{amp}	-0.125	-0.125	-0.125	-0.125	-0.125	-0.125
z_{amp}	-0.125	-0.125	-0.125	-0.125	-0.125	-0.125
$\tilde{u}$	0	0	0	0	0.125	0.25
$\tilde{k}/\pi$	—	—	—	—	1	1
δ_t	0	0	0	0	5	5
L	4	4	4	4	4	4
W	1	1	1	1	1	1
D	4	4	4	4	4	4
Δt	0.005	0.005	0.005	0.005	0.005	0.005
N_{time}	2501	2501	2001	2001	2501	2501
N_{iter}	2	2	2	2	2	2
I_{max}	97	97	97	73	97	97
J_{max}	25	25	25	19	25	25
K_{max}	97	97	97	73	97	97
γ	0.20	0.20	0.40	0.20	0.20	0.20

TABLE 1. Data for a pair of vortex tubes impinging on a free surface. Fully nonlinear free-surface boundary conditions are used on the top of the computational domain and free-slip boundary conditions are used on the sides and bottom. The spatial accuracy is either fourth- or sixth-order. The Reynolds, Froude, and Weber numbers are respectively denoted by Re, Fr, and We. The initial core radius and peak vorticity are denoted by r_c and ω_c. The mean position of the vortex core is centred at (x_0, z_0). The initial amplitudes of the sinusoidal perturbations in the core's position are x_{amp} and z_{amp}. $\tilde{u}$ is the initial r.m.s. velocity of the fluctuating velocity field, and $\tilde{k}$ is the wavenumber where the maximum occurs in the spectrum of the fluctuating velocity field (see Appendix C). δ_t is the adjustment time, which is described in Appendix D. The lengths of the computational domain along the x-, y-, and z-axes are respectively L, W, and D. The time step is Δt. The number of time steps is N_{time}, and the number of iterations required to solve the nonlinear elliptic equations is N_{iter} (see Appendix B). The number of grid points along the x-, y-, and z-axes are respectively I_{max}, J_{max}, and K_{max}. The parameter γ specifies the grid resolution in the free-surface boundary layer as explained in Appendix A.

spectra are defined in Appendix E to measure the accuracy of the numerical simulations. Figure 3 plots the energy spectra of the velocity components for four different laminar simulations at a time when the primary vortex tube is strongly interacting with the free surface.

The first numerical simulation (Run 1 of table 1) uses a sixth-order approximation and $97 \times 25 \times 97$ grid points to resolve the fluid volume, with five grid points in the free-surface boundary layer based on a boundary-layer thickness $\delta = O(Re^{-\frac{1}{2}})$. The second simulation (Run 2) is fourth order and uses the same grid resolution as the first simulation. The third simulation (Run 3) is fourth order and uses $97 \times 25 \times 97$ grid points to resolve the fluid volume, with $2\frac{1}{2}$ grid points in the boundary layer. The fourth simulation (Run 4) is also fourth-order and uses $73 \times 19 \times 73$ total grid points with five grid points in the boundary layer. As is evident in figure 3, all of the numerical simulations agree very well except at the highest wavenumbers. The only evidence of an energy pileup occurs where the energy density is 16 decades lower than
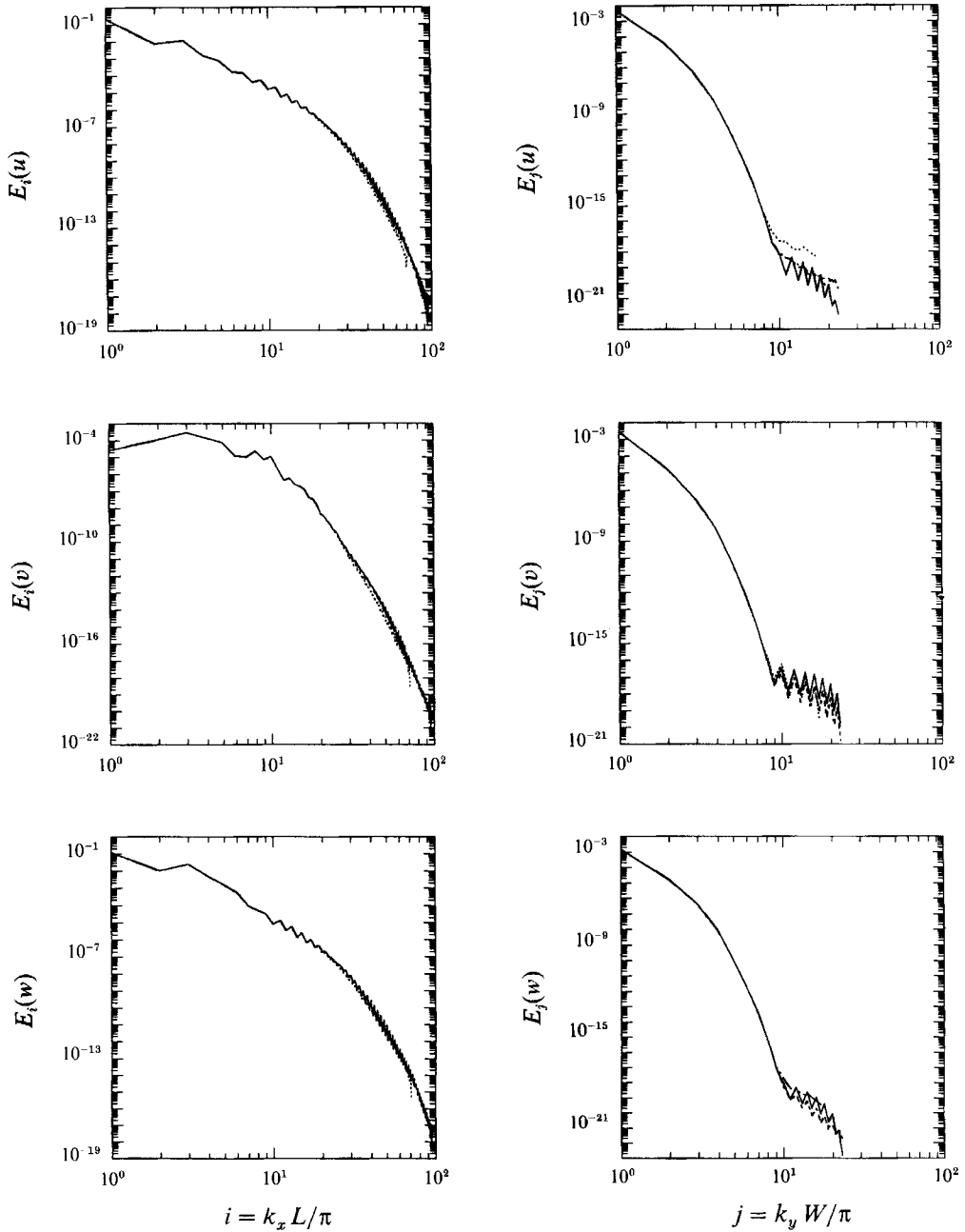
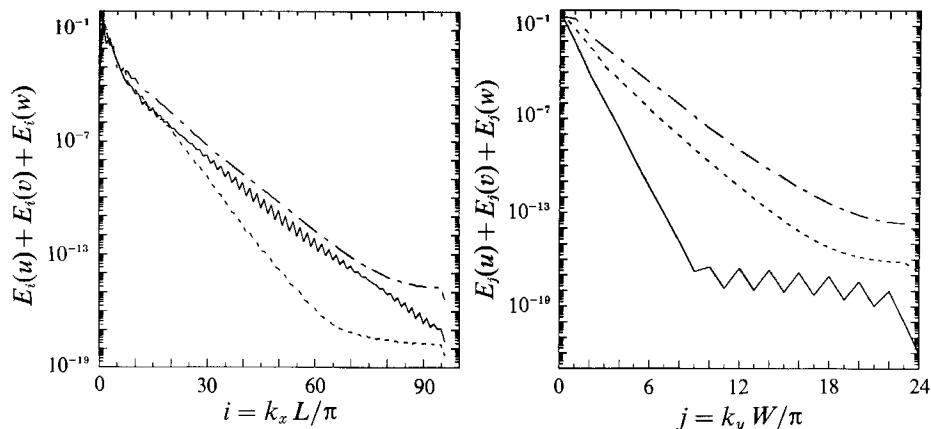**FIGURE 3.** One-dimensional energy spectra of the velocity components, plotted for four different numerical simulations at time $t = 10$: ——, ———, —·—, and ------, denote Runs 1, 2, 3, and 4 of table 1. The curves are indistinguishable except at the highest wavenumbers.

the energy density at lowest wavenumbers. The energy pileup is probably due to accumulation of round-off errors.

Figure 4 compares the energy spectra of the laminar and transitional simulations. The r.m.s. velocities of the fluctuating velocity fields are 0.125 and 0.25 for the two transitional simulations (Runs 5 and 6 of table 1). The initial kinetic energies of the fluctuating velocity fields are approximately 25 and 75% of that of the primary

FIGURE 4. One-dimensional energy spectra of the total velocity, plotted for three different numerical simulations at time $t = 10$: —, - - - -, and — - — denote Runs 1, 5, and 6 of table 1.
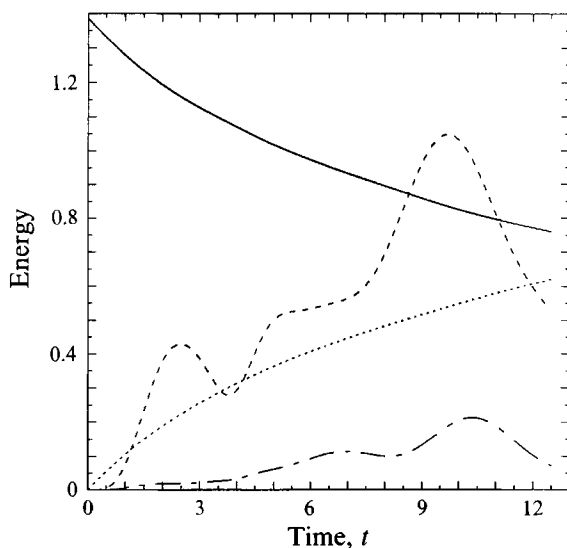
FIGURE 5. The energy balance of a laminar vortex tube impinging a free surface. —, — — —, — - — -, and - - - - - denote the kinetic energy (E_{uu}), the potential energy $(100 E_{\eta\eta})$, the negative of the work done to surface tension $(-100 W_{\text{T}})$, and the negative of the work due to viscous stresses $(-W_{\nu})$.

vortex tube so that the total energies of the transitional simulations are initially greater than those of the laminar simulation. Turbulent interactions decrease the energy densities at the lowest wavenumbers so that for time $t \geqslant 10$ the kinetic energies of the transitional simulations are less than those of the laminar simulation. This effect is observed in figure 4(a, b) for the zero wavenumbers, where the laminar simulation has an energy density that is greater than or equal to the energy densities of the transitional simulations. Figure 4(a, b) also shows that the transitional simulations have a slight energy pileup at the highest wavenumbers.

Figures 5 and 6 show the energy balances based on (27) of the laminar and transitional simulations. The transitional simulations, unlike the laminar simulation, use an atmospheric forcing term to reduce the impulse of the vortical pressure (see Appendix D). For all of the simulations the potential energy $(E_{\eta\eta})$ is less than 2% of
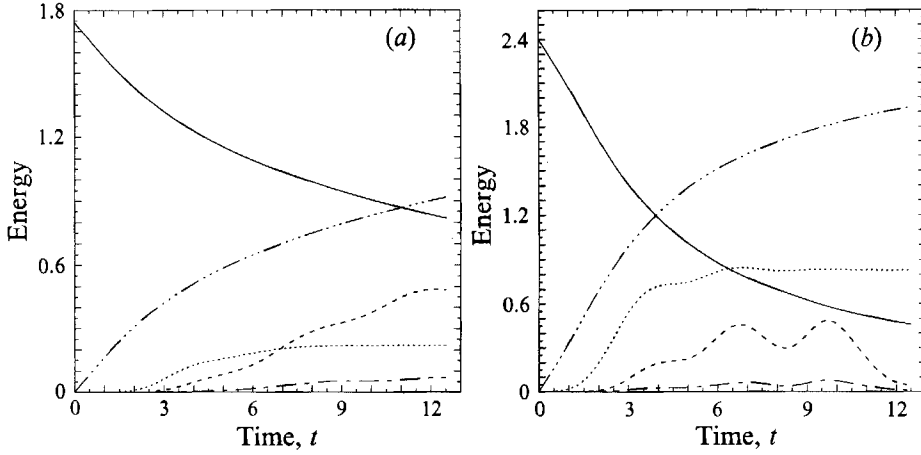
FIGURE 6. The energy balances of transitional vortex tubes impinging a free surface, (a) Run 5 and (b) Run 6. —, — — —, — · — · —, · · · · · ·, and — · · — · · denote the kinetic energy (E_{uu}), the potential energy $(100\,E_{\eta\eta})$, the negative of the work due to surface tension $(-100\,W_{\mathrm{T}})$, the negative of the work due to atmospheric forcing $(-100\,W_{pa})$, and the negative of the work due to viscous stresses $(-W_{\nu})$.
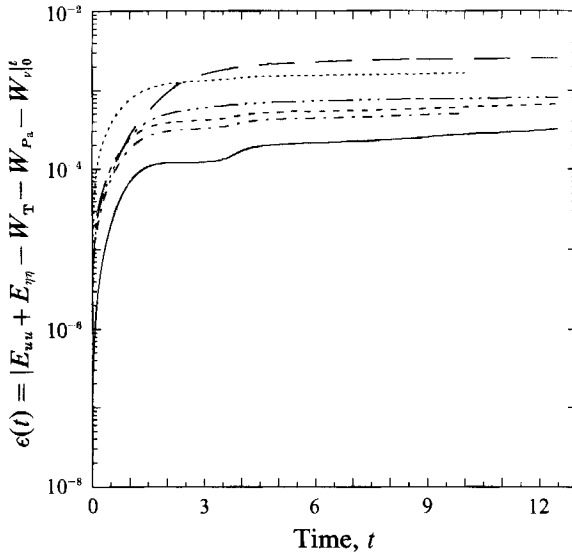

FIGURE 7. The integrated absolute error in the energy as a function of time. —, — — —, — · — · —, · · · · · ·, — · · — · · , and — — — — denote Runs 1–6 of table 1.

the kinetic energy (E_{uu}), and the work due to surface tension (W_T) is about 20% of the potential energy. The work due to the atmospheric forcing (W_{P_a}) in the transitional simulations initially grows rapidly but then levels off due to the exponential attenuation in (D1). Viscous dissipation (W_{ν}) is the dominant effect, especially for the transitional simulations.

The integrated absolute error in the conservation of energy

$$\epsilon(t) = |E_{uu} + E_{\eta\eta} - W_T - W_{P_a} - W_{\nu}|_0^t$$

is plotted in figure 7 for the numerical simulations listed in table 1. All of the numerical simulations conserve energy to within 0.1% relative to the initial kinetic energy. The sixth-order simulation (Run 1) conserves energy best. Run 3 with $2\frac{1}{2}$ grid
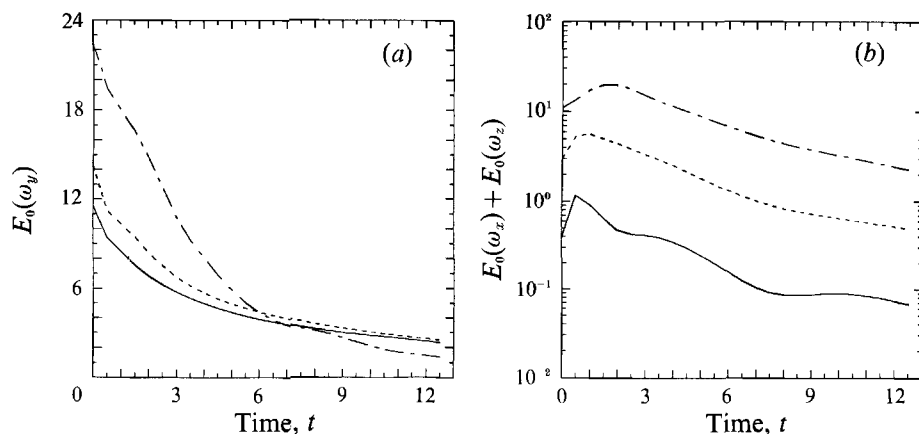
FIGURE 8. The creation and attenuation of enstrophy. (a) The axial and (b) the cross-axis components. —, ——, and —·—· denote Runs 1, 5, and 6 of table 1.

	$\eta_{\min}$	$\eta_{\max}$	$|\eta_x|_{\max}$	$|\eta_{xx}|_{\max}$	$|\eta_y|_{\max}$	$|\eta_{yy}|_{\max}$
Run 1	-0.128	0.0781	0.323	2.78	0.0201	0.0696
Run 5	-0.0708	0.0535	0.119	0.573	0.0182	0.147
Run 6	-0.0604	0.0793	0.172	0.645	0.0772	0.320

TABLE 2. Free-surface elevations and radii of curvature for three different runs

points in the free-surface boundary layer conserves energy better than Run 2, which has 5 points. This result indicates that for clean free surfaces numerical accuracy depends equally on the grid resolutions of the fluid's interior and the free-surface boundary layer.

Figure 8 shows the axial and cross-axis components of enstrophy. The axial vorticity steadily decreases as a function of time. Based on two-dimensional vortices with Gaussian cores, the rate of attenuation of the axial enstrophy is

$$E_0(\omega_y) \propto (1 + 4t\nu_e/(\pi r_c^2))^{-2},$$

where t is the time, r_c is the core radius, and ν_e is an effective viscosity. For the laminar simulation $\nu_e \approx 0.0052$, which corresponds to a Reynolds number of 200. For the two transitional simulations $\nu_e \approx 0.0059$ and 0.0094, so the most energetic transitional simulation (Run 6 of table 1) is almost twice as viscous as the laminar simulation.

For $t \leqslant 1$ there is a rapid increase in the cross-axis vorticity. This increase corresponds to the inviscid instability that Sarpkaya & Suthon (1990) observed in their experiments. Dommermuth's (1992) numerical simulations of vortex tubes impinging on a wall show a similar initial increase in the cross-axis enstrophy. However, unlike the wall simulations, the free-surface simulations show no evidence of a secondary instability for $t \gg 1$. An increase in cross-axis vorticity would typically occur as strong secondary vortices are shed from the wall, but for the results that are illustrated in figure 8(b) the free-surface displacement is not large enough to generate strong secondary vortices.

Table 2 illustrates that the shedding of secondary vorticity does not occur despite strong free-surface nonlinearity. We observe that the maximum and minimum free-

surface elevations and the radii of curvature are the same order as the core radius, and the maximum wave slopes are approximately 75% of the Stokes two-dimensional breaking-wave criterion. The extrema of the transitional simulations (Runs 5 and 6) are generally less than the laminar simulation (Run 1) because the adjustment procedure that is used in the transitional simulations eliminates spurious standing waves. In a ship wake the Froude number of a characteristic eddy is two orders of magnitude less than the present numerical simulations (Dommermuth & Yue 1990), such that the free-surface nonlinearity would also be much less. This evidence supports Hirsa *et al.*'s (1990) conclusion that surface contamination may be the dominant mechanism for generating secondary vorticity in the far wake of a ship. However, more studies are required at higher Reynolds numbers and lower Froude numbers to determine if changes in the free-surface curvature and slope can lead to the generation of secondary vorticity in ship wakes.

As a vortex tube interacts with itself and its neighbours, sheets of helical vorticity are spiralled off. The origin of the sheets appears to be the result of an inviscid instability that is initiated by large changes in curvature along the axes of the primary vortex tubes. When the wavelength of the instability is very short, the sheets of helical vorticity manifest themselves as beads of cross-axis vorticity. Similar bead-like structures are observed in Sarpkaya & Suthon's (1991) dye studies (see their figures 8 and 9) and Sarpkaya's (1992) dye studies (see his figure 3). Figure 9(*a–g*) (plate 1) shows the isosurfaces of the vorticity for a laminar vortex tube impinging a clean free surface. Figure 9(*a–c*) illustrates the initial unwinding the cross-axis vorticity. As is evident from the flat appearance of the free surface, the initial instability is a sub-surface phenomenon that is not influenced by the presence of a free surface, which also agrees with the observations of Sarpkaya & Suthon (1990). As the cross-axis vortex tubes rotate around and translate with the primary vortex tube, they reconnect with their images across the centreplane ($x = 0$). Sarpkaya & Suthon's (1990, 1991) observations and Dommermuth's (1992) computations show that the reconnections occur at the front stagnation point of the Kelvin oval.

The free surface rises above the primary vortex tube to form an oval shape and secondary vorticity is shed in the scar region as seen in figure 9 (*c,d*). The formation of ovals and scars is a two-dimensional phenomenon. As we will see, the formation of striations and whirls by the cross-axis vortex tubes is three-dimensional. The influence of the primary vortex tubes and the cross-axis vortex tubes on the free surface is similar to the influence of a cam on the valves of an engine. The axle of the cam represents the primary vortex tube, and the rocker arms of the cam represent the cross-axis vortex tubes. The eccentric rotation of the cam induces a reciprocating motion to the valves, just as the orbit of the cross-axis vortex tubes around the primary vortex tubes causes striations to appear on the free surface. Figure 9(*c*) shows a fully developed cam vortex that is partially entrained in a wave crest.

Figure 9(*d–f*) shows that the cross-axis vortex tubes disconnect from the centreplane and reconnect with the free surface. The reconnection process is similar to Saffman's (1990) theoretical model and Melander & Hussain's (1988) cut-and-connect model. As the vortex pair rises up the centreplane toward the free surface, the velocities induced by the vortex images above the free surface cause the vortex pair to split, and the two primary vortex tubes move apart parallel to the free surface. The cross-axis vortex tubes are stretched, and their cores flatten to form an elliptical cross-section (see figure 9*d*). A new stagnation point forms in front of the primary vortex tube on the free surface. At this stagnation point a contact zone is
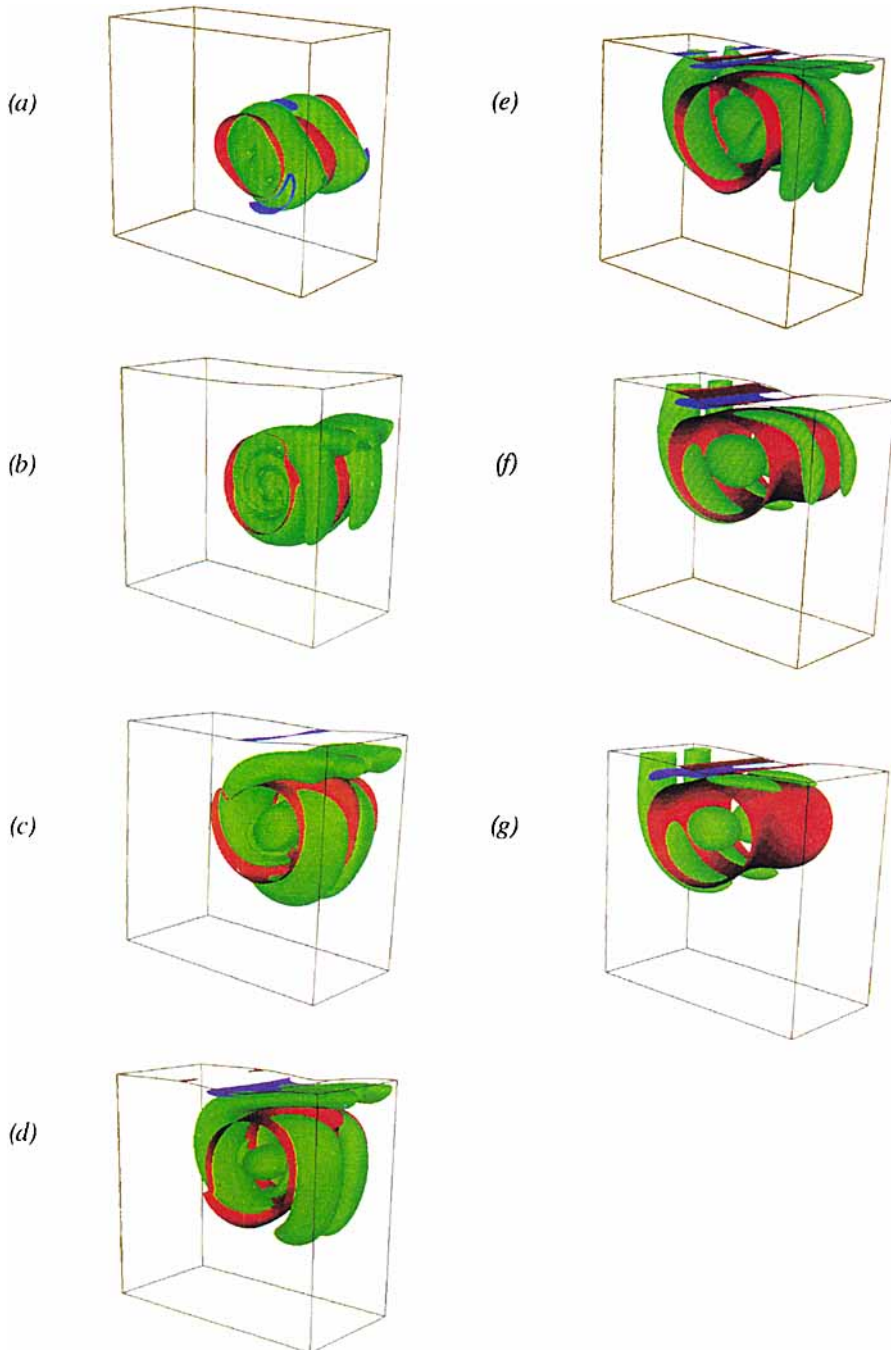
FIGURE 9. A laminar vortex tube impinging a free surface. The isosurfaces of the cross-axis vorticity $(\omega_x^2+\omega_z^2)^{\frac{1}{2}}=0.2$, the positive axial vorticity $\omega_y=0.2$, and the negative axial vorticity $\omega_y=-0.2$ are denoted by green, red, and blue colours at different instants of time: *(a)* $t=0$, *(b)* $t=2$, *(c)* $t=4$, *(d)* $t=6$, *(e)* $t=8$, *(f)* $t=10$, and *(g)* $t=12$. The black lines outline the edges of the computational domain, which includes the free surface. The images have been reflected about the (x,z)-plane. This flow visualization study is based on the results of Run 1 of table 1.
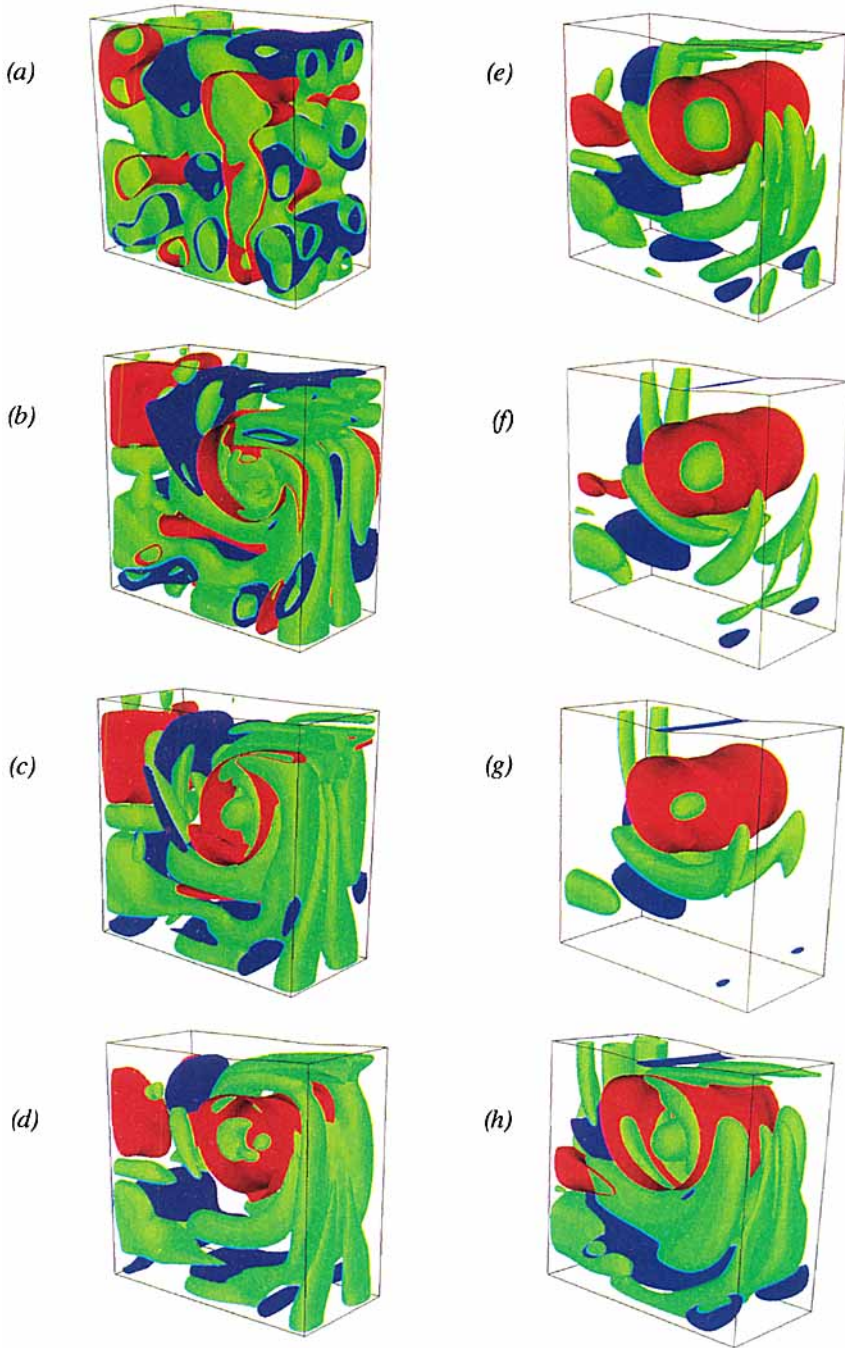
FIGURE 10. A transitional vortex tube impinging a free surface. The isosurfaces of the cross-axis vorticity, the positive axial vorticity, and the negative axial vorticity are denoted by green, red, and blue colours at different instants of time. The isosurface levels are 0.5 for parts *(a)* − *(g)* and 0.2 for part *(h)*. The time instants are: *(a)* t=0, *(b)* t=2, *(c)* t=4, *(d)* t=6, *(e)* t=8, *(f)* t=10, *(g)* t=12, and *(h)* t=12. This flow visualization study is based on the results of Run 5 of table 1.

formed, and vorticity diffusion in the contact zone leads to the formation of a bridge (see figure 9e). The vortex lines in the bridge are normal to the free surface. The reconnection is complete in figure 9(f). While the reconnection is occurring, secondary vorticity is shed from the outboard side of the scar region. In figure 9(d–f) the red bands in the scar region are the boundary layers of the blue bands of shed secondary vorticity. The reconnection of cross-axis vorticity occurs on the outboard sides of the vortex pair where Sarpkaya & Suthon (1990, 1991) observe the formation of whirls and dimples (see figure 1).

The vortex structure that is illustrated in figure 9(g) has a snail-like shape. The point where a cross-axis vortex tube is perpendicular to the free surface corresponds to the 'mouth' of a 'snail' vortex. The other cross-axis vortex tube corresponds to the 'back' and 'base' of a snail vortex. The striations that form above the base of a snail vortex are similar to the slime trails that are left by late-night visits of Southern California's notorious garden-variety snails. The spheroids that form in the centre of a snail vortex, which is the centre of the primary vortex tube, are called cup-shaped features by Rogers & Moser (1991). The cups occur in the regions of high vortex stretching that are produced by the strain fields of the primary and cross-axis vortex tubes. In figure 9(f, g) the cross-axis vortex tube that is on the back portion of the snail vortex is moving toward the front stagnation point where it too will connect with the free surface.

Figure 10(a–h) (plate 2) shows the isosurfaces of vorticity for a transitional vortex tube impinging a clean free surface (see Run 5 of table 1). Except for part (h), all of the plots in figure 10 use a higher isosurface level than the laminar simulation to eliminate the high wavenumber components. This artifice had also been applied to the more energetic transitional simulation (Run 6), but only remnants of the primary vortex tube could be identified.

As illustrated in figure 10(a–h), the primary vortex tube organizes the fluctuating velocity field, and we also observe that the fluctuating velocity field decays much faster than the primary vortex tube. The numerous cross-axis vortex tubes that spin around the primary vortex tube are similar to the tentacle-like sheets that peel off a turbulent vortex (see figures 7 and 8 of Sarpkaya 1992). For a transitional vortex tube, just like a laminar vortex tube, the reconnections with the centreplane and the free surface tend to occur at the front stagnation point of the Kelvin oval. Figures 10(b–e) and 10(e–g) respectively show reconnection with the centreplane and the free surface. Figure 10(h) shows the isosurfaces at a lower level. Comparing figure 10(h) to figure 9(g) shows that the transitional vortex tube has twice as many reconnections with the free surface as the laminar vortex tube. Figure 10(b–d) also shows that the cross-axis vortex tubes amalgamate at the stagnation points on the centreplane. Amalgamation is not observed on the free surface because the cross-axis vortex tubes have lost too much energy. Sarpkaya's (1992) numerical and experimental studies of the whirls generated by a turbulent vortex tube suggest that amalgamation can give a reverse energy cascade, whereby energy is transferred from high to low wavenumbers.

Figures 11 and 12 show contour plots of free-surface quantities for the laminar and transitional simulations. The primary vortex tube is moving from the left ($x = 0$) to the right ($x = 4$) side of the page. Figure 11(a) shows that undulations in the free-surface elevation occur as a laminar vortex tube impinges a free surface. The similarities between figures 11(a) and 11(b) show that these undulations may be related to the vortical pressure term in the free-surface boundary conditions (see (14)). The rotation of the cross-axis vortices around the primary vortices (see figures
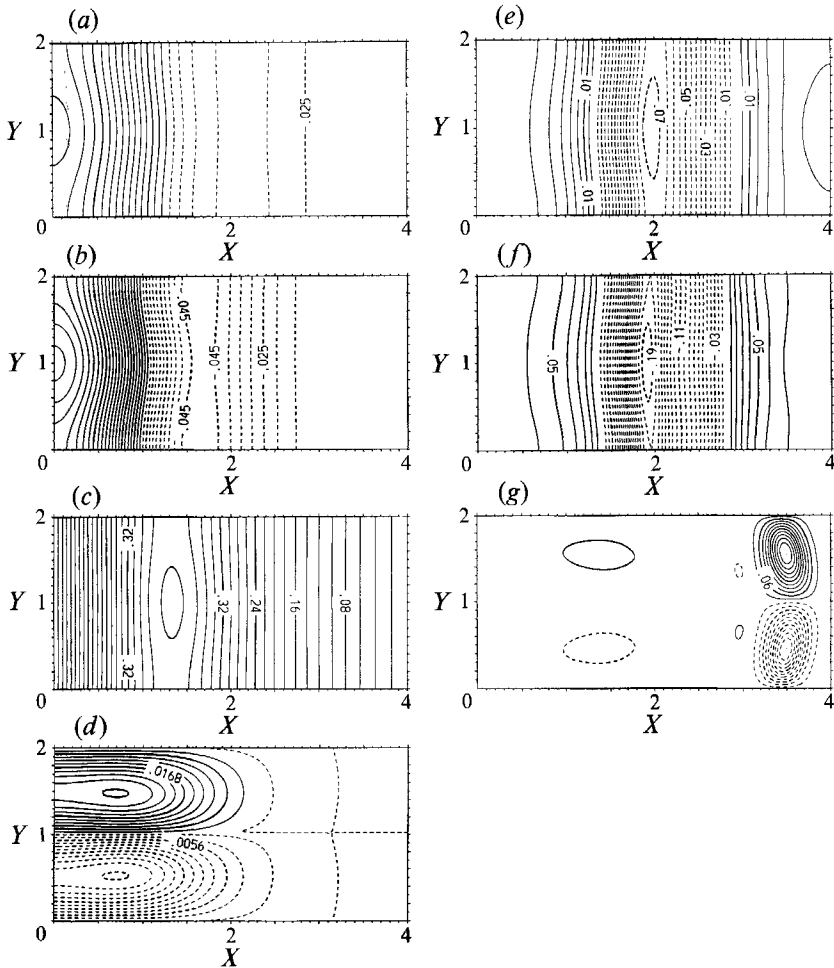
FIGURE 11. Contours of free-surface quantities for a laminar vortex tube: (a) η, (b) P, (c) u, (d) v, corresponding to $t = 2.5$, and (e) η, (f) P, (g) ω_z, corresponding to $t = 12.5$. The contour extremes and increments are: (a) -0.025 to 0.07 by 0.005; (b) -0.045 to 0.11 by 0.005; (c) 0 to 0.4 by 0.02; (d) -0.028 to 0.028 by 0.0028; (e) -0.07 to 0.035 by 0.005; (f) -0.19 to 0.07 by 0.01; and (g) -0.42 to 0.42 by 0.04. Solid and dashed lines respectively denote positive and negative quantities. These contours plots have been reflected about the (x, z)-plane based on the results of Run 1 of table 1.

9 and 10) causes axial variations in the vortical pressure and unsteady undulations in the free-surface elevation. The contour plots of the free-surface velocities in figure 11 (c, d) show that water particles are convected away from the centreplane of the vortex pair due to influence of the primary vortices, and down the sides of the undulations due to the cross-axis vortices. The similarity of these results to Sarpkaya & Suthon's (1991) observations (see their figure 6a) suggests that these undulations are related to the formation of striations.

Figure 11 (e–g) shows that a pair of whirls eventually forms at the tips of the undulations where the cross-axis vortices reconnect with the free surface, which also agrees with Sarpkaya & Suthon's observations (see their figure 12). Figure 11 (e, f) shows that the contours of the free-surface elevation and the vortical pressure are still correlated, but neither the free-surface elevation nor the vortical pressure appears to be strongly affected by the reconnection of the cross-axis vortices with the
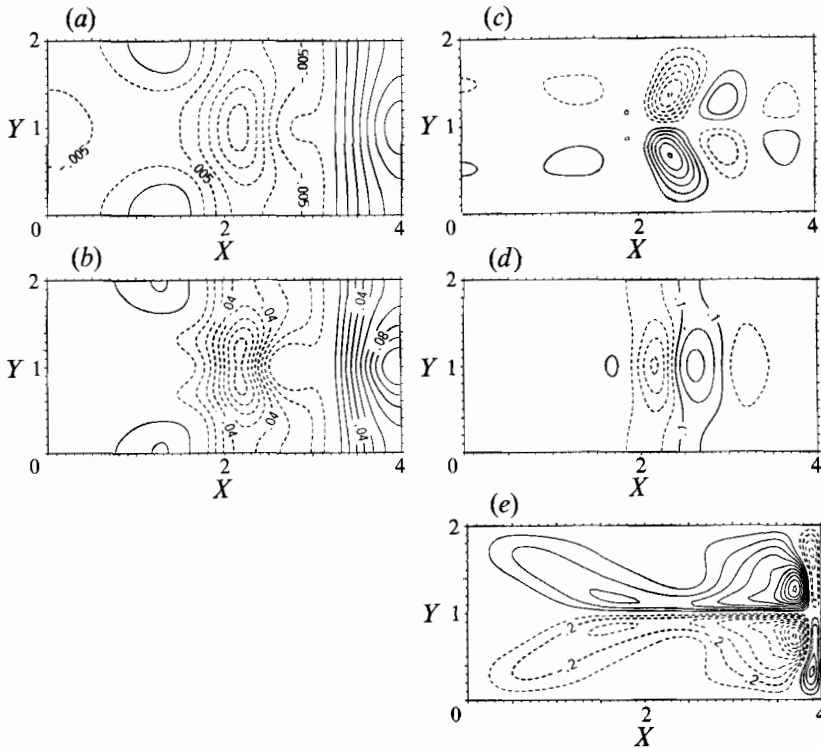
FIGURE 12. Contours of free-surface quantities for a transitional vortex tube. (a) η, (b) P, (c) ω_x, (d) ω_y, (e) ω_z, corresponding to time $t = 12$. The contour extremes and increments are: (a) -0.025 to 0.035 by 0.005; (b) -0.08 to 0.1 by 0.01; (c) -0.24 to 0.24 by 0.04; (d) -0.7 to 0.5 by 0.2; and (e) -1 to 1 by 0.1. These contour plots are based on the results of Run 6 of table 1.

free surface. Based on Dommermuth's (1992) numerical simulations of vortex tubes impinging on a wall, the strength of the cross-axis vortices is increased by the shedding of secondary vorticity. Strong vortex shedding does not occur in the present free-surface simulations. If vortex shedding did occur and the cross-axis vortices got stronger, then dimples and upwellings could form on the free surface. Some possible mechanisms for generating secondary vorticity and strengthening the cross-axis vorticity include increasing the Reynolds number, the Froude number, or the surface contamination.

The contour plots in figure 12 show the signature of a pinched vortex tube whose axis is parallel to the free surface. For this transitional simulation, just like the preceding laminar simulation, the free-surface elevation (figure 12a) and the vortical pressure (figure 12b) are well correlated. The contours of the vorticity components in figure 12(c–e) show that the free-surface disturbance at ($x \approx 2$, $y \approx 1$) is due to a vortex tube whose axis is parallel to the free surface rather than normal. Flow visualization studies indicate that a pinched vortex tube grazes the free surface near the centre of the contour plots where the disturbances are located. This event appears to be similar to the *splat* models that are described in Hunt (1984) and Leighton *et al.* (1991). Although the primary vortex tube is torn apart in this transitional simulation, its remnants sweep cross-axis vorticity to the point where whirls form in the laminar simulations (see figure 12e for $x \geqslant 3$). The pressure disturbance of the four whirls causes a single upwelling in the free-surface elevation.
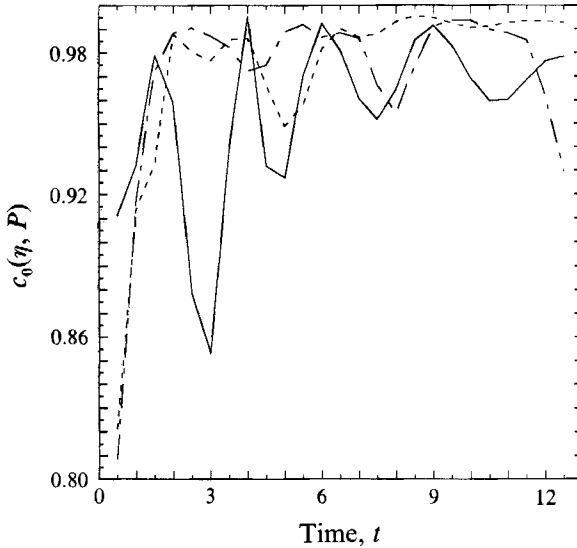
FIGURE 13. Cross-correlation coefficient of the free-surface elevation and the vortical pressure:
—, — — —, and — · — · — denote Runs 1, 5, and 6 of table 1.

The preceding examples of laminar and transitional vortex tubes impinging on a clean free surface suggest that the free-surface elevation is well correlated with the vortical pressure. Let l_e and u_e denote the length and velocity of a characteristic eddy, then the timescale of the vortical and wavy motions are respectively $t_v \sim l_e/u_e$ and $t_w \sim (l_e/g)^{\frac{1}{2}}$, where g is gravity. The ratio of these two timescales is given in terms of the Froude number: $Fr = t_w/t_v = u_e/(gl_e)^{\frac{1}{2}}$. At low Froude numbers, when the timescale of the vortical motions is longer than the timescale of the wavy motions, we expect the free-surface elevation to balance with the vortical pressure $\eta \approx F_r^2 P$. The contour plots in figures 11 and 12 tend to support this balance of terms.

A cross-correlation coefficient c_0 is defined in Appendix E (see (E3)), and the coefficients are plotted in figure 13. The laminar simulation (Run 1) and the transitional simulations (Runs 5 and 6) have very strong correlations between the free-surface elevation and the vortical pressure ($c_0 \geq 0.95$ for $t \geq 4$). The correlation of the transitional simulations are initially poor because of the adjustment procedure, but for $t \geq 2$ the transitional simulations have higher correlation coefficients than the unadjusted laminar simulation. The small oscillations in the correlation coefficients correspond to long standing waves.

The balancing between the gravity and vortical pressure terms indicates that the response of the free surface is hydrostatic – no dispersive waves are generated. If the transitional simulations had not been adjusted, the impulse of the vortical pressure would have generated standing waves, and these standing waves would have obscured the true hydrostatic response of the free surface.

5. Summary

As observed by Sarpkaya (1986) and Sarpkaya & Suthon (1990, 1991), an interesting aspect of vortex tubes impinging on a clean free surface is the reconnection of normal vorticity with the free surface. The numerical simulations illustrate that the cross-axis vorticity which is wrapped around the primary vortex tubes can connect normally with the free surface.

As each primary vortex tube interacts with itself and its neighbours, sheets of helical vorticity are shed. The origin of the sheets of helical vorticity appears to be the result of an instability that is initiated by large changes in curvature along the axes of the primary vortex tubes. The helical vortex sheets are initially tightly wound around the primary vortex tubes, but eventually the sheets evolve into beads of cross-axis vorticity. The cross-axis vorticity connects across the centreplane of the vortex pair at the front stagnation point of the Kelvin oval. As the pair of vortex tubes rises up to the free surface, an oval bounded by two steep troughs, i.e. scars, forms above the centre of the pair. The formation of the oval and the scars is a two-dimensional phenomenon that is caused by the primary vortex tubes. The vortex pair begins to split apart due to the velocity that is induced by the image of the vortex pair above the free surface.

The connections of cross-axis vorticity across the centreplane are broken, and the cross-axis vorticity reconnects with the free surface. This breaking and reconnection process causes unsteady oscillations in the free-surface elevation, i.e. striations, that are superimposed on top of the two-dimensional features. For laminar flows, whirls form where cross-axis vorticity connects normally with the free surface. The scars and dimples that form in transitional free-surface flows are due to fluctuations in the vortical pressure, which are caused by the passing of eddys close to the free surface. A dimple on the free surface can form above an eddy that is either parallel or normal to the free surface.

Appendix A. Mapping

The z-coordinate $(\eta \geqslant z \geqslant -D)$ is mapped onto a flat plane by using the transformation

$$\hat{z} = (z+D)/(\eta+D), \qquad (A\,1)$$

where D is the depth of the computational domain. The grid is also stretched along the $\hat{z}$-axis to resolve the boundary layer on the free surface. The positions of the grid points are denoted by $\hat{z}_k$ for $1 \leqslant k \leqslant K_{\text{tot}}$, where $K_{\text{tot}} = 2K_{\text{max}} - 1$. The rotational velocity $(\mathcal{U})$ is solved on the odd grid points (K_{max} points), and the rotational pressure (P) is solved on the even grid points ($K_{\text{max}} - 1$ points). The grid spacing is prescribed in terms of a Hermitian polynomial:

$$\hat{z} = \sum_{i=0}^{6} a_i \left(\frac{k-1}{K_{\text{tot}}-1}\right)^i, \qquad 1 \leqslant k \leqslant K_{\text{tot}}, \qquad (A\,2)$$

where the coefficients a_i of the Hermitian polynomial $H(k)$ are assigned as follows:

$$H(1) = 1, \quad H(K_{\text{tot}}) = 0, \quad H_k(1) = -\gamma Re^{-\frac{1}{2}}/(2D)$$

$$H_{kk}(1) = 0, \quad H_{kk}(K_{\text{tot}}) = 0, \quad H_{kkk}(K_{\text{tot}}) = 0, \, H_{kkkk}(K_{\text{tot}}) = 0.$$

γ is the desired fraction of the laminar boundary-layer thickness $(\delta = Re^{-\frac{1}{2}})$ at the free surface for the rotational velocity grid. Note that the grid spacing is uniformly

spaced along the $\hat{z}$-axis for the potential (ϕ) because it does not have a boundary layer, and K_{max} points are used to discretize ϕ. The grid spacing is also uniformly spaced in the horizontal plane for all physical quantities. Furthermore, in the horizontal plane the rotational pressure is staggered relative to the rotational velocities, the velocity potential, and the free-surface elevation. Extrapolation and interpolation between the different grids is performed using fourth- and sixth-order schemes depending on the order of the approximation.

Appendix B. Iterative solutions

Let $\hat{z} = F(x, y, z, t) = (z+D)/(\eta+D)$ account for the mapping of the free surface onto a flat plane, and let $k = G(\hat{z})$ account for the grid stretching, if any, at the kth index. (If there is no grid stretching, then $G_{\hat{z}} = 1 - K_{\mathrm{max}}$ and $G_{\hat{z}\hat{z}} = 0$.) If $\phi^m(x, y, k, t)$ denotes the mth iterant solution to the velocity potential, then the following arrangement of terms provides an efficient algorithm for solving Laplace's equation with exact free-surface boundary conditions:

$$\phi_{xx}^{m+1} + \phi_{yy}^{m+1} + (G_{\hat{z}}^2/D^2)\,\phi_{kk}^{m+1} + (G_{\hat{z}\hat{z}}/D^2)\,\phi_k^{m+1} = -(F_x^2 + F_y^2 + F_z^2 - (1/D^2))\,G_{\hat{z}}^2\,\phi_{kk}^m$$
$$-2F_y\,G_{\hat{z}}\,\phi_{yk}^m - 2F_x\,G_{\hat{z}}\,\phi_{xk}^m - ((F_{xx} + F_{yy})\,G_{\hat{z}} + (F_x^2 + F_y^2 + F_z^2 - (1/D^2))\,G_{\hat{z}\hat{z}})\,\phi_k^m, \quad \text{(B 1)}$$

where the Fourier transform with respect to x and y leads to a set of one-dimensional Poisson equations that are solved using LU-decomposition. The source term on the right-hand side of the equation is updated, and the solution scheme repeats itself. Generally, only one to two iterations are required in the Navier–Stokes code because the first approximation is very close to the exact solution. The iterative solution of the Poisson equation for the rotational pressure is similar, but the solvability condition (7) must be enforced during each iteration.

Appendix C. The fluctuating velocity field

The initial fluctuating velocity field ($\mathcal{U}_f$) is expressed in terms of a vector velocity potential ($\mathcal{A}_f = (a, b, c)$) to ensure that $\mathcal{U}_f$ is solenoidal. If the free-surface elevation is initially zero and no shear stresses are applied on the free surface, and free-slip boundary conditions are used on the sides and the bottom of the computational domain, then the appropriate Fourier decomposition of $\mathcal{A}_f$ is

$$
\left.
\begin{aligned}
a &= \sum_{i=0}^{I_{\mathrm{max}}-1} \sum_{j=1}^{J_{\mathrm{max}}-1} \sum_{k=1}^{K_{\mathrm{max}}-1} a_{ijk} \cos(k_x x) \sin(k_y y) \sin(k_z z), \\
b &= \sum_{i=1}^{I_{\mathrm{max}}-1} \sum_{j=0}^{J_{\mathrm{max}}-1} \sum_{k=1}^{K_{\mathrm{max}}-1} b_{ijk} \sin(k_x x) \cos(k_y y) \sin(k_z z), \\
c &= \sum_{i=1}^{I_{\mathrm{max}}-1} \sum_{j=1}^{J_{\mathrm{max}}-1} \sum_{k=0}^{K_{\mathrm{max}}-1} c_{ijk} \sin(k_x x) \sin(k_y y) \cos(k_z z),
\end{aligned}
\right\} \quad \text{(C 1)}
$$

where $k_x = i\pi/L$, $k_y = j\pi/W$, and $k_z = k\pi/D$, and L, W, and D are respectively the length, width, and depth of the computational domain. Based on Orszag & Pao (1974), the shape of the fluctuating velocity spectrum is chosen as

$$S(\kappa) \sim \kappa^4 \exp\left(-2\kappa^2/\tilde{k}^2\right), \quad \text{(C 2)}$$

where $\kappa^2 = k_x^2 + k_y^2 + k_z^2$ and $\tilde{k}$ is the wavenumber where the maximum occurs in the

spectrum. The kinetic energy is equally divided among the non-zero Fourier coefficients $(a_{ijk}, b_{ijk}, c_{ijk})$ of the vector velocity potential using the formula

$$\delta_i \delta_j \delta_k (a_{ijk}^2 + b_{ijk}^2 + c_{ijk}^2) = \kappa^2 \exp(-2\kappa^2/\tilde{k}^2), \tag{C 3}$$

where $\delta_i = 1$ for $i = 0$ or $i = I_{\max} - 1$ and $\delta_i = \frac{1}{2}$ otherwise. δ_j and δ_k are similarly defined, and the signs of the Fourier coefficients are calculated using a pseudo-random number generator. The initial fluctuating velocity field is calculated using $\mathcal{U}_f = \nabla \times \boldsymbol{\psi}_f$, and the fluctuating velocity field is scaled such that the kinetic energy after the projection of $\mathcal{U}_f$ onto a solenoidal field is equal to $\frac{3}{2}LWD\tilde{u}^2$, where $\tilde{u}$ is the r.m.s. velocity.

Appendix D. The adjustment problem

The vortical pressure that is induced by the fluctuating velocity field will generate spurious high-frequency waves on the free surface unless the flow field is given sufficient time to adjust – even if the initial free-surface elevation is zero. Weather prediction techniques like nonlinear normal mode initialization (Baer & Tribbia 1977) are not practical because of the complex coupling between the free-surface elevation and the potential and vortical velocity fields. A simpler approach is to reduce the impulses of the vortical pressure and the normal component of the viscous stresses by applying an atmospheric forcing term. The atmospheric forcing is prescribed as follows:

$$P_a = \hat{P}_a \exp(-t^2/\delta_t^2), \tag{D 1}$$

where $\hat{P}_a$ is the amplitude of the pressure and δ_t is the adjustment time. To minimize transients, the adjustment time is chosen to be greater than the wave period of the longest standing wave that is permitted in the computational domain. The amplitude $\hat{P}_a$ is prescribed in terms of the vortical pressure and the normal component of the viscous stress:

$$\hat{P}_a = P - \frac{2}{Re(\eta_x^2 + \eta_y^2 + 1)}(W_z + \phi_{zz} - (W_y + V_z + 2\phi_{yz})\eta_y - (W_x + U_z + 2\phi_{xz})\eta_x$$
$$+ (V_y + \phi_{yy})\eta_y^2 + (U_x + \phi_{xx})\eta_x^2 + (V_x + U_y + 2\phi_{xy})\eta_x\eta_y). \tag{D 2}$$

In some numerical simulations the potential and free-surface elevation may be prescribed in terms of fully nonlinear Stokes waves. In lieu of determining the exact solution to the vortical flow in the free-surface boundary layer of the Stokes waves, we can use a similar procedure to reduce the impulse of the tangential stresses on the free surface.

Appendix E. Spectral analysis with a free surface

Two one-dimensional energy spectra of a three-dimensional function $F(x, y, z, t)$ are defined as

$$E_i(F) = \frac{1}{2}W \int_0^1 d\hat{z} \sum_{j=0}^{J_{\max}-1} \delta_j \hat{f}_{ij}^2(\hat{z}, t), \qquad E_j(F) = \frac{1}{2}L \int_0^1 d\hat{z} \sum_{i=0}^{I_{\max}-1} \delta_i \hat{f}_{ij}^2(\hat{z}, t), \tag{E 1}$$

where $\delta_i = 1$ for $i = 0$ or $i = I_{\max} - 1$ and $\frac{1}{2}$ otherwise. δ_j is similarly defined. $\hat{f}_{ij}$ is the Fourier decomposition in the horizontal plane in terms of cosine and/or sine series of $(\eta(x, y, t) + D)^{\frac{1}{2}}F(x, y, \hat{z}, t)$, where the factor $(\eta + D)^{\frac{1}{2}}$ accounts for the mapping from the

z- to the $\hat{z}$-coordinate system. Based on the initial conditions (28), E_i and E_j respectively measure the energy densities of the vortex pair in the spanwise and axial directions. Corresponding to these one-dimensional energy spectra, an expression for the total energy is

$$E_0(F) = \tfrac{1}{2}LW \int_0^1 d\hat{z} \sum_{i=0}^{I_{max}-1} \delta_i \sum_{j=0}^{J_{max}-1} \delta_j \hat{f}_{ij}^2(\hat{z}, t). \qquad (E\,2)$$

The cross-correlation coefficient of two free-surface quantities (A and B) is defined as

$$c_0(A,B) = \sum_{i=0}^{I_{max}-1} \delta_i \sum_{j=0}^{j_{max}-1} \delta_j a_{ij}(t) b_{ij}(t) \bigg/ \left(\sum_{i=0}^{I_{max}-1} \delta_i \sum_{j=0}^{J_{max}-1} \delta_j a_{ij}^2(t) \sum_{i=0}^{I_{max}-1} \delta_i \sum_{j=0}^{J_{max}-1} \delta_j b_{ij}^2(t) \right)^{\frac{1}{2}},$$
$$(E\,3)$$

where a_{ij} and b_{ij} are the Fourier coefficients.

REFERENCES

BAER, F. & TRIBBIA, J. J. 1977 On complete filtering of gravity modes through nonlinear initialization. *Mon. Wea. Rev.* **12**, 1536–1539.

CROW, S. 1970 Stability theory for a pair of trailing vortices. *AIAA J.* **8**, 2172–2179.

DOMMERMUTH, D. G. 1991 The viscous interactions of a pair of vortex tubes with a free surface. *Science Applications International Corporation, Tech. Rep.* SAIC-91/1326.

DOMMERMUTH, D. G. 1992 The formation of U-shaped vortices on vortex tubes impinging on a wall with applications to free surface. *Phys. Fluids* A **4**, 757–769.

DOMMERMUTH, D. G. & YUE, D. K. P. 1990 A numerical study of three-dimensional viscous interactions of vortices with a free surface. In *Proc. 18th Symp. on Naval Hydrodyn., Ann Arbor* pp. 727–788. National Academy of Sciences, Washington, DC.

HIRSA, A. 1990 An experimental investigation of vortex pair interaction with a clean or contaminated free surface. Ph.D. thesis, University of Michigan, Dept. of Aero. Engng.

HIRSA, A., TRYGGVASSON, G., ABDOLLAHI-ALIBEIK, J. & WILLMARTH, W. W. 1990 Measurement and computations of vortex pair interaction with a clean or contaminated free surface. In *Proc. 18th Symp. on Naval Hydrodyn., Ann Arbor*, pp. 521–532. National Academy of Sciences, Washington, DC.

HIRT, C. W., NICHOLS, B. D. & ROMERO, N. C. 1975 SOLA-A numerical solution algorithm for transient fluid flows. *Los Alamos Scientific Lab. Rep.* LA-5852.

HUNT, J. C. R. 1984 Turbulence structure and turbulent diffusion near gas-liquid interfaces. In *Gas Transfer at Water Interfaces* (ed. W. Brutsaert & G. H. Jirka), pp. 67–82. D. Reidel.

LEIGHTON, R. I., SWEAN, T. F., HANDLER, R. A. & SWEARINGEN, J. D. 1991 Interaction of vorticity with a free surface in turbulent open channel flow. In *Proc. 29th Aerospace Sciences Meeting, Reno, NV, AIAA* 91–0236.

LUGT, H. J. & OHRING, S. 1992 The oblique ascent of a viscous vortex pair toward a free surface. *J. Fluid Mech.* **236**, 461–476.

MELANDER, M. V. & HUSSAIN, F. 1988 Cut-and-connect of two antiparallel vortex tubes. In *Studying Turbulence using Numerical Databases – II, Proc. 1988 Summer Program* Rep. CTR-S88, pp. 257–286. NASA Ames Research Center & Stanford University.

OHRING, S. & LUGT, H. J. 1991 Interaction of a viscous vortex pair with a free surface. *J. Fluid Mech.* **227**, 47–70.

ORSZAG, S. A. & PAO, Y. H. 1974 Numerical computation of turbulent shear flows. In *Proc. Symp. on Turbulent Diffusion in Environmental Pollution* (ed. F. N. Frenkiel & R. E. Mann), pp. 225–236. Academic.

RAI, M. M. & MOIN, P. 1991 Direct simulations of turbulent flow using finite-difference schemes. *J. Comput. Phys.* **96**, 15–53.

ROGERS, M. M. & MOSER, R. D. 1991 The three-dimensional evolution of a plane mixing layer. Part 1 : The Kelvin–Helmholtz rollup. *NASA Ames Research Center, NASA Tech. Memo* 103856.

SAFFMAN, P. G. 1990 A model of vortex reconnection. *J. Fluid Mech.* **212**, 395–402.

SARPKAYA, T. 1985 Surface signatures of trailing vortices and large scale instabilities. In *Proc. Colloq. on Vortex Breakdown (Sonderforschungsbereich, 25)*, pp. 145–187. University of Aachen.

SARPKAYA, T. 1986 Trailing-vortex wakes on the free surface. In *Proc. 16th Symp. on Naval Hydrodyn.* pp. 38–50. National Academy of Sciences, Washington, DC.

SARPKAYA, T. & HENDERSON, D. O. 1984 Surface disturbances due to trailing vortices. *Naval Postgraduate School, Tech. Rep.* NPS-69-84-004.

SARPKAYA, T. 1992 Three-dimensional interactions of vortices with a free surface. In *Proc. 30th Aerospace Sciences Meeting & Exhibit, Reno, NV, AIAA* 92–0059.

SARPKAYA, T. & SUTHON, P. 1990 Scarred and striated signature of a vortex pair on the free surface. In *Proc. 18th Symp. on Naval Hydrodyn., Ann Arbor*, pp. 503–520. National Academy of Sciences, Washington, DC.

SARPKAYA, T. & SUTHON, P. 1991 Interaction of a vortex couple with a free surface. *Exps. Fluids* **11**, 205–217.

SPREITER, J. R. & SACKS, A. H. 1951 The rolling up of the trailing vortex sheet and its effect on the downwash behind wings. *J. Aero. Sci.* **18**, 21–32.

ZAKHAROV, V. E. 1968 Stability of periodic waves of finite amplitude on the surface of a deep fluid. *J. Appl. Mech. Tech. Phys.* **9**, 190–194. (English transl.)